Experimental Mechanics
DOI 10.1007/s11340-014-9893-z

# Static Laboratory Earthquake Measurements with the Digital Image Correlation Method

**V. Rubino · N. Lapusta · A.J. Rosakis · S. Leprince · J.P. Avouac**

Received: 17 October 2013 / Accepted: 1 April 2014


**Abstract** Mapping full-field displacement and strain changes on the Earth's surface following an earthquake is of paramount importance to enhance our understanding of earthquake mechanics. Currently, aerial and satellite images taken pre- and post-earthquake can be processed with sub-pixel correlation algorithms to infer the co-seismic ground deformations (e.g., [1, 2]). However, the interpretation of this data is not straightforward due to the inherent complexity of natural faults and deformation fields. To gain understanding into rupture mechanics and to help interpret complex rupture features occurring in nature, we develop a laboratory earthquake setup capable of reproducing displacement and strain maps similar to those obtained in the field, while maintaining enough simplicity so that clear conclusions can be drawn. Earthquakes are mimicked in the laboratory by dynamic rupture propagating along an inclined frictional interface formed by two Homalite plates under compression (e.g., [3]). In our study, the interface is partially glued, in order to confine the rupture before it reaches the ends of the specimen. The specimens are painted with a speckle pattern to provide the surface with characteristic features for image matching. Images of the specimens are taken before and after dynamic rupture with a 4 Megapixels resolution CCD camera. The digital images are analyzed with two software packages for sub-pixel correlation: VIC-2D (Correlated Solutions Inc.) and COSI-Corr [1]. Both VIC-2D and COSI-Corr are able to characterize the full-field static displacement of the experimentally produced dynamic shear ruptures. The correlation analysis performed with either software clearly shows (i) the relative displacement (slip) along the frictional interface, (ii) the rupture arrest on the glued boundaries, and (iii) the presence of wing cracks. The obtained displacement measurements are converted to strains, using non-local de-noising techniques; stresses are obtained by introducing Homalite's constitutive properties. This study is a first step towards using the digital image correlation method in combination with high-speed photography to capture the highly transient phenomena involved in dynamic rupture.

**Keywords** Digital image correlation · Dynamic rupture · Earthquake mechanics · Remote sensing

V. Rubino (✉) · A.J. Rosakis
Graduate Aerospace Laboratories, California Institute of Technology, 1200 East California Blvd, Pasadena, CA 91125, USA
e-mail: vito.rubino@caltech.edu

N. Lapusta
Division of Engineering and Applied Science, California Institute of Technology, 1200 East California Blvd, Pasadena, CA 91125, USA

N. Lapusta · S. Leprince · J.P. Avouac
Division of Geological and Planetary Science, California Institute of Technology, 1200 East California Blvd, Pasadena, CA 91125, USA

## Introduction

Observing earthquake-induced deformation in nature is a challenging but important task. Measuring displacements, strains, and stresses on the Earth's surface due to an earthquake would reveal key features of the rupture mechanics. Such measurements would also enable us to quantify the pattern of ground shaking in the near field and its decay away from the fault line, which is directly linked to the damage level. The existing ground-based seismic networks have a fine temporal resolution but rather limited spatial distribution. The best existing networks have average inter-station distances of the order of 10 km (e.g. [4]). On the other hand, remote sensing based on radar interferometry or on air- and spaceborne optical images offers a much denser spatial coverage, and it has been successfully applied to tectonics and other geological processes (e.g. [1, 2, 5–7]).

The advantage of air- and spaceborne images is that they can be analyzed with optical flow methods, which offer sub-

Published online: 22 May 2014

pixel accuracy. COSI-Corr (Co-registration of Optically Sensed Images and Correlation) software package implements image-correlation techniques optimized for co-registration of pairs of images, and it is capable of measuring displacements with a maximum uncertainty of about 1/200 of a pixel [1]. An example of the displacement and strain maps obtained by correlating pairs of pre- and post-earthquake aerial images, for the 1992 Mw 7.3 Landers earthquake in California, is shown in Fig. 1 [2]. While such maps offer insight into the co-seismic ground deformations, there are many unclear aspects due the inherent complexity of a natural earthquake.

Motivated by developing a laboratory analogue of air- and spaceborne remote sensing techniques, this study employs the digital image correlation method in the laboratory earthquake setup which has been previously used to reproduce some key dynamic rupture phenomena such as supershear transition, bimaterial effect, and pulse-like rupture propagation [3, 8–13]. The diagnostics currently employed in this laboratory earthquake setup is focused either on temporally accurate velocity measurements (based on laser velocimetry and representing a laboratory analogue of seismometers) but with a sparse spatial resolution (up to three measurement stations in one experiment) or on photoelasticity, which provides a full-field technique to measure maximum shear stress. The current laboratory configuration is not capable of a spatially continuous measurement of displacements, strains and stresses. While photoelaestic measurements of maximum shear stress are useful to explain many key aspects of the rupture process, they do not provide all components of stress and strain, and they are not easy to compare with the field data (Fig. 1).

The goal of this study is to obtain full-field displacement measurements and compute strain and stress changes during ruptures in the laboratory, mimicking the measurements and information that would be obtained from air- and spaceborne optical measurements. This setup offers a unique opportunity to observe up-close the mechanics of laboratory earthquake rupture and yet maintains enough simplicity so that clear conclusions can be drawn. Enriching this setup with the digital image correlation technique holds promise for exploring new dynamic rupture phenomena.

The digital image correlation method is an optical technique to analyze images of an object, recorded in a digital form, to obtain full-field deformation measurements [14]. It was first applied to experimental mechanics by Peters and Ranson [15]; Sutton et al. [16]; Chu et al., [17] and since then it has experienced a rapid growth in the number of applications. Surface displacements are computed by tracking the motion and/or deformation of image subsets containing a characteristic pattern. The digital image correlation method has been successfully used to study crack problems and to measure fracture parameters both statically and dynamically (e.g. [18–24]). In this work, we employ DIC to map the static displacement, stress and strain changes associated with the propagation of a dynamic mode II crack.

In this study, the laboratory earthquake setup [3] is modified to include constant intensity white-light illumination to mimic the sun light, while the specimen surface is coated with a characteristic random pattern to reproduce the texture of the surface topography. Images are taken before and after a laboratory experiment by a CCD digital camera. The images are subsequently analyzed with digital image correlation techniques to characterize the full-field static displacement of a dynamic rupture. Two digital image correlation software packages are employed in this study: COSI-Corr [1], developed in the context of satellite image analysis, and VIC-2D (Correlated Solutions Inc.), developed in the context of experimental mechanics, and the results are compared. Both cross-correlation methods perform the search of a correlation peak by optimizing a suitably defined correlation function. The main difference between the two approaches is that VIC-2D performs this search in the space domain, while COSI-Corr operates in the Fourier domain. Traditionally, space-domain methods were regarded as slower compared to Fourier-domain methods. However, subsequent implementations using the Newton–Raphson or Levenberg-Marquardt methods have made space-domain implementations significantly faster than their earlier versions [25, 26]. In this paper, we employ the 2D implementation of the digital image correlation method (2D-DIC) since, in the laboratory earthquake experiment, the out-of-plane displacements are less than a third of the in-plane displacements [27].

This study constitutes the first step towards developing a full-field technique of measuring dynamic displacements, strains, and stresses, in which a high-speed camera system will be employed to capture the transient deformation. The dynamic measurements would be a laboratory analogue of the space optical seismometer [28]. The outline of the paper is as follows. First, the laboratory earthquake experiment is described, and then the image acquisition, processing, and post-processing procedures are explained. The static displacement, strain, and stress measurements of a dynamic rupture are presented and discussed for two examples, one with a rupture that propagated at sub-Rayleigh speeds and the other with a rupture that transitioned to supershear speeds. The method error is subsequently discussed, followed by concluding remarks.

## Laboratory Earthquakes and the Digital Image Correlation Method

### How to Make Earthquakes in the Laboratory

The experimental setup mimics a fault in the Earth's crust prestressed both in compression and shear (e.g.

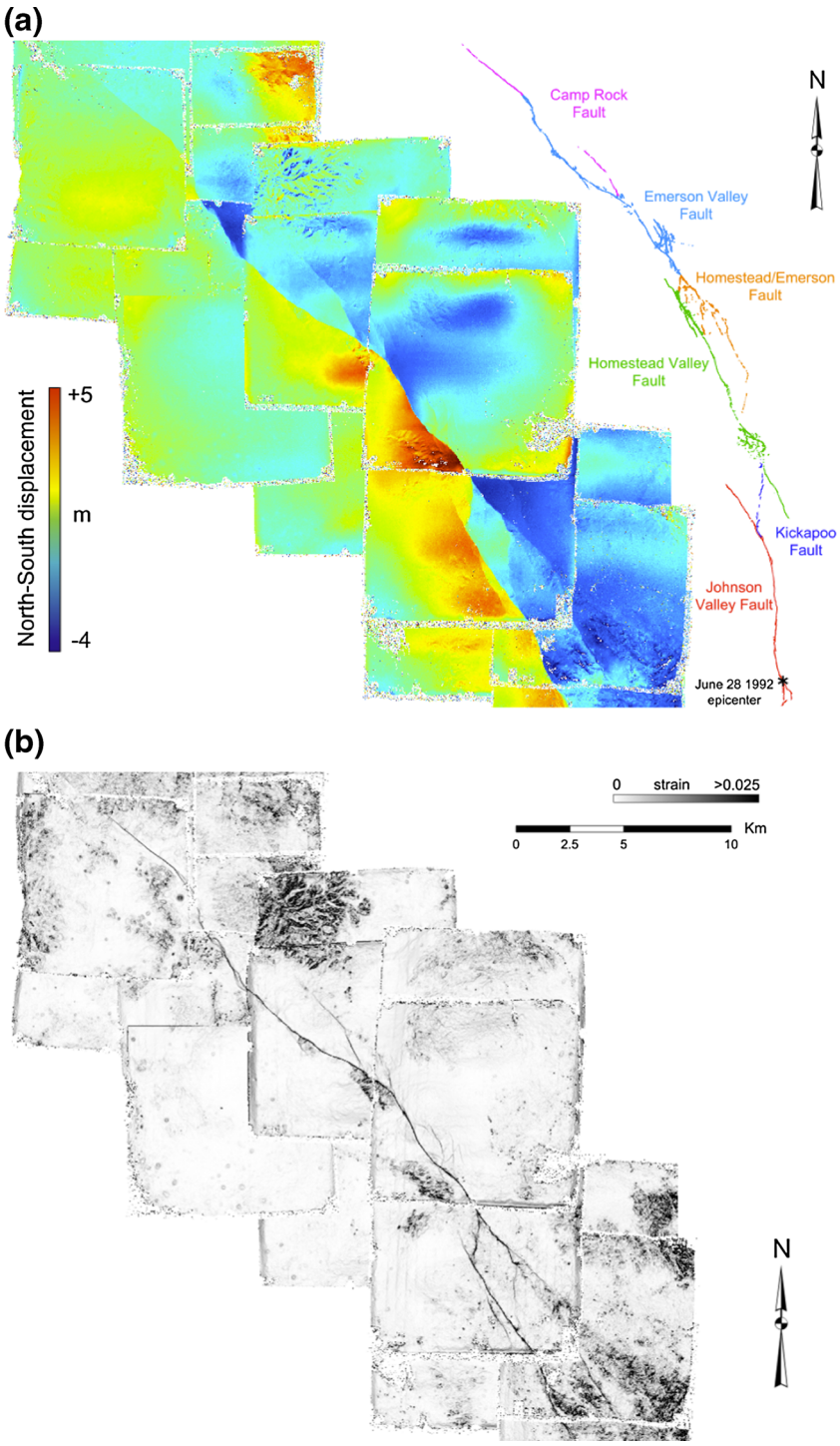


**Fig. 1** (**a**) North–south component of displacement field for the 1992, Mw 7.3 Landers earthquake in California. Pairs of aerial images (USGS-NAPP 1989–1995) are correlated and composed in a mosaic of displacement maps. (**b**) Strain field obtained from the displacement maps shown in (a). Adapted from [2]

[3, 10]). A rectangular plate of Homalite-100, a transparent stress birefringent material, with the dimensions of 360 mm × 180 mm × 10 mm, is cut using computer-numerical-control (CNC) into two quadrilaterals, introducing a fault plane with an inclination angle $\alpha$ (Fig. 2(a)). A unidirectional pressure $P$ is applied to the upper and lower edges of the quadrilateral plate assembly (Fig. 2(b)). The parameters $P$ and $\alpha$ determine the resolved shear traction $\tau_0 = P \sin\alpha \cos\alpha$ and normal traction $\sigma_0 = P \cos^2\alpha$ on the fault. The non-dimensional shear prestress given by $f_0 = \tau_0/\sigma_0 = \tan\alpha$ indicates how close the interface is to failure according to the Coulomb criterion. Because the static friction coefficient of the interface is approximately 0.6, the inclination angle $\alpha$ is chosen to be 30° or less in order to prevent sliding during the static

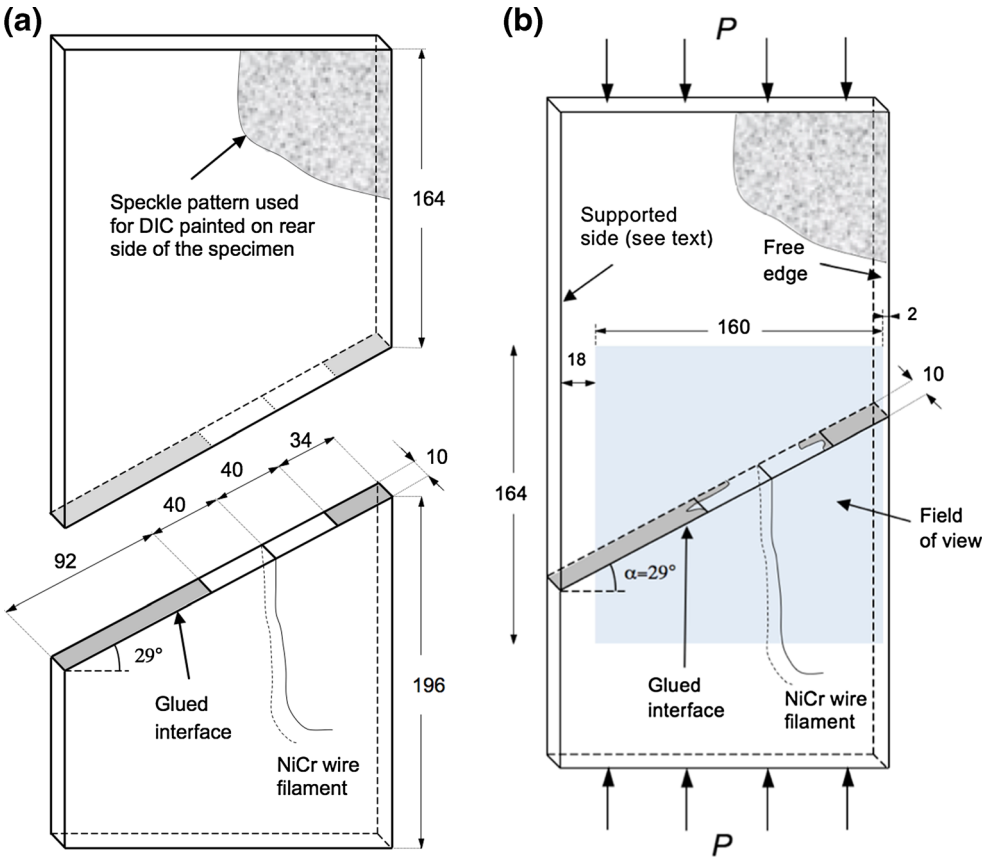


**Fig. 2** Schematics of the test specimen geometry and loading configuration. Two static compressive stress levels are applied to obtain sub-Rayleigh and supershear rupture speeds respectively: $P$=5 MPa and $P$=15 MPa. (**a**) Nominal dimensions (in mm) of test specimen and glued interface. (**b**) Loading configuration of the test assembly and typical profile of the glued region observed in the manufactured specimen. The transparent Homalite specimens are decorated with a random speckle pattern to produce a characteristic texture for the digital image correlation

preloading stage. The specimens considered in this study have an inclination angle $\alpha$=29° . Two static compressive stress levels are studied: $P$=5 and $P$=15 MPa.

In a number of past studies, both lateral edges of the Homalite specimen are free (e.g., [3, 10, 12, 13, 27]). In this study, we employ the configuration of Gabuchian et al. [29] (Fig. 2) in which, to prevent buckling, the left vertical edge of the specimen is supported. The support is achieved by two opposite sets of eleven M13 bolts which are lightly screwed along a vertical line positioned 10 mm from the left edge. The right edge of the specimen is free (Fig. 2(b)). While the bolts have the purpose of constraining the out-of-plane motion of the Homalite specimen, the measurements presented in subsequent sections reveal that they also end up constraining some in-plane motion. Since we study the final static displacement of a dynamic rupture (i.e. the displacements after the rupture has arrested), these boundary conditions affect the presented results. In contrast, the boundary conditions at the left or right edge do not affect the study of Gabuchian et al. [29], or any previous studies in similar experimental setups (e.g., [3, 10, 12, 13, 27]), since they consider the propagation of a dynamic rupture before stress wave reflections from the boundaries reach the field of observation.

To remove defects from CNC cutting, the mating surfaces of the quadrilateral plates are first polished to a near optical grade finish. The surfaces are subsequently roughened by using a micro-bead blasting treatment with abrasive glass beads having diameters in the range of 43–89 μm [13, 27]. This surface preparation procedure ensures repeatability of the dynamic frictional rupture experiments. Two end portions of the interface are covered with a film of glue, in order to confine the rupture before it reaches the ends of the specimen.

To achieve nucleation of dynamic rupture, a NiCr wire, 79 μm in diameter, is placed at the desired rupture nucleation site along the interface of the two Homalite test sections. The NiCr wire is connected to a 1.5 kV capacitor bank through alligator clips and copper wire. The sudden electrical disintegration of the NiCr wire introduces a local pressure release on the fault plane, which triggers a dynamic shear rupture, due to resolved shear stress exceeding locally the frictional strength of the interface. The rupture is dominated by 2D in-plane slip similar to large strike-slip earthquakes that saturate the entire seismogenic depth.

In laboratory earthquake studies [3, 10, 12, 13, 27], dynamic photoelasticity, in conjunction with high speed photography, is used to capture full field images of the transient dynamic event. An expanded and well-collimated laser beam is used to illuminate the transparent specimen. A pair of circular polarizers, one in front and one behind the Homalite specimen, forms the basis of a dark-field polariscope assembly. The resulting isochromatic fringe patterns correspond to isocontours of maximum shear stress $\tau_{max}=(\sigma_1-\sigma_2)/2$, where

$\sigma_1$ and $\sigma_2$ are the principle stresses at each location. In addition to acquiring full field photoelastic images, laser velocimeters are used to measure particle velocity history at selected points on the surface of the specimen [30, 31]. The instruments record a specific velocity component which can be fault-parallel, fault-normal, or out-of-plane (normal to the face of the specimen), and they are capable of tracking particle velocities of up to 10 m/s.

While photoelasticity gives the full-field maximum shear stress, the individual values of the principal stress components remain unknown. Laser velocimetry provides measurements of high temporal resolution (of the order of picoseconds), but it has low spatial resolution. Typically up to three velocimeters are employed in this experimental setup.

## Developing Full-Field Imaging of Laboratory Earthquakes by the Digital Image Correlation Method

One way of obtaining a full-field characterization of the in-plane displacement and strain field is by employing the Digital Image Correlation (DIC) technique. The advantage of this technique is in its ability to measure small surface displacements with sub-pixel accuracy, which is achieved by processing grey-scale data comprising the images of randomly speckled patterns applied to the surface of a test specimen. In this study, the DIC technique is employed in the laboratory earthquake setup in order to measure the static deformation of a dynamic crack.

The specimens are first coated with a uniform layer of Krylon flat white paint. Second, a random black-speckle pattern, which provides the surface with characteristic features for image matching, is obtained by coarse-spraying Krylon black paint. In order to capture large displacement gradients, a small feature size is required, to maximize the information content in each comparison window. At the same time, features which are too small would result in aliasing. A number of patterns with speckles of different sizes have been produced by controlling the distance of the spray can to the target. These patterns have been imaged and analyzed to determine which pattern minimized the measurement error (see section "Accuracy of the DIC Measurements for Laboratory Earthquakes"). The average feature size has been selected to be in the range of 3–6 pixels. This feature size ensures that optimum pattern matching is performed [14].

Digital images of the specimens are taken with a 2,048 × 2,048 pixel resolution JAI Pulnix TM-4200CL camera and a 55 mm lens. A Photron light is used to provide a steady light source during the exposure time. The spatially continuous mapping of the fault-parallel and fault-normal displacement fields is obtained by processing two static images, one taken before and one after a laboratory earthquake (section "Analysis of Displacement, Strain, and Stress Fields for Sub-Rayleigh and Supershear Rupture Cases"). In addition, a series of nominally identical images of the specimen are taken. The displacement fields inferred from these images are used to quantify the error associated with the measurement technique (section "Accuracy of the DIC Measurements for Laboratory Earthquakes"). An example of two typical images taken before and after a laboratory earthquake is shown in Fig. 3. In order to measure the pixel size, pictures are taken with a millimeter paper on the target. The pixel size is determined by the number of pixels per millimeter. In all images presented here, there are 124 pixels in 10 mm or 12.4 pixels per millimeter. Hence, the pixel size is 80.6 μm. The image taken before dynamic rupture features a wire with alligator clips connected to the NiCr filament (*left panel*). As the NiCr filament bursts during the rupture nucleation procedure, the alligator clips and the rest of the wire fall off, and consequently they are not visible in the image taken after the dynamic rupture has propagated (*right panel*).

The digital images are analyzed with two software packages: VIC-2D (Correlated Solutions Inc.) and COSI-Corr [1]. There are two key parameters to be selected for each image correlation analysis: the subset size and the step size. To perform a correlation, image sets are broken down into subsets. Each subset contains a gray level signature. This characteristic information is compared between subsets in correlating two images. The subset size is the size of such image regions over which pattern matching is performed. The subset size controls the spatial resolution of the correlation maps. Larger subsets contain more information and facilitate pattern matching. However, larger subsets also imply averaging deformation over larger regions with consequent reduction of spatial resolution. Correlation analyses have been performed with a range of subset sizes. The optimum subset size, which offers the best compromise between spatial averaging and correlation accuracy, is 32 × 32 pixels. This subset size implies that displacements are averaged across regions of 2.6 × 2.6 mm, since the pixel size is 80.6 μm. A typical subset is shown in the insets of Fig. 3. Once pattern matching is performed on a given subset, the analysis proceeds to the next subset. The step size is the size of the pixel increment from one subset to the following. For a given spatial resolution, the step size determines the density of data in the output. Small step sizes give dense data sets at the expense of computational time, while large steps may result in fields which are too sparse. In this study, a step size of 4 pixels is found to optimize data density and computational time.

Two reference systems are introduced (Fig. 3). The reference system denoted as $x_1$'- $x_2$' has its axes oriented parallel to the edges of the specimen; this is the reference frame in which the DIC software outputs the displacement fields. To facilitate the interpretation of the full-field deformation maps, it is convenient to introduce a reference system with axes $x_1$and $x_2$ being parallel and perpendicular to the experimental fault line, respectively.

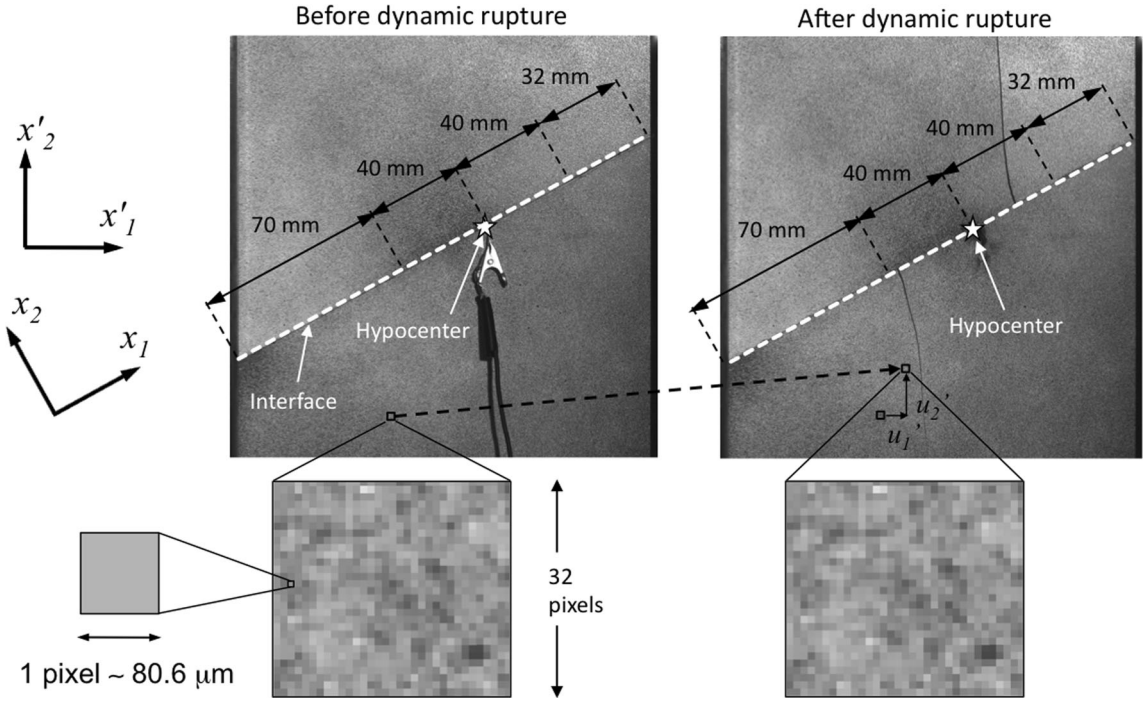


**Fig. 3** Images of the test specimen before and after a laboratory earthquake. These digital images are correlated to infer the full-field displacement. The insets show a typical subset magnified and the associated pixel size: 1 pixel ~80.6 mm

## Data Post-Processing: Displacement Filtering, Strain and Stress Calculation

The horizontal and vertical components of displacement computed by the correlation analysis are denoted by $u_1'$ ($x_1'$, $x_2'$) and $u_2'$ ($x_1'$, $x_2'$) respectively (Fig. 3). The displacement fields are subsequently exported from the DIC software for plotting and post-processing with a different package (Matlab, The MathWorks Inc.). An example of the horizontal and vertical displacement fields obtained from a typical correlation performed with COSI-Corr is presented in Fig. 4(a) and (b). The displacement magnitude is expressed in pixels. In this example, the externally applied load before the dynamic rupture is $P$=5 MPa. VIC-2D gives very similar results.

The inferred displacement fields (Fig. 4(a) and (b)) contain a significant amount of noise. The presence of this noise affects the strain calculation process. To illustrate this, it is useful to plot the displacement fields along selected paths. For example, the displacement field $u_1'$ ($x_1'$, $x_2'$) is tracked along Path #1 and Path #2 (marked in Fig. 4(a)) in Fig. 5(a) and (b) (*blue curves*), respectively. While these curves do capture key rupture features, such as the overall displacement gradients and the displacement jump across the ruptured interface, the noise level of the displacement fields does not allow for accurate strain computation.

Several approaches have been developed to compute strains from noisy full-field displacement data (e.g. [32–34]). One typical approach is to filter displacements with a Gaussian filter. However, Gaussian filters are not ideal for problems with interfaces, since they achieve signal smoothing by averaging the gray level content of each pixel with that of the neighboring pixels. The averaging is performed regardless of the difference between the gray level of the pixel to be averaged and that of the surrounding pixels. For instance, in a displacement map containing a discontinuity at an interface, a pixel at the boundary of the interface would be averaged with neighboring pixels on the opposite side of the interface. This concept is illustrated in Fig. 4(c) and (d) where the displacement fields obtained in VIC-2D (very similar to Fig. 4(a) and (b)) have been filtered using a local filter with a Gaussian window of 39x39 pixels. Local smoothing is a suitable approach when operating over continuous displacement fields (Fig. 5(a)) but it has the negative effect of losing sharp edges and signal discontinuities, such as displacement jumps across the interface of a mode II rupture (Fig. 5(b)). In contrast, the Non-Local-Means Filter [35–37], also referred to as NL-means filter, considers a set of pixels (neighborhood) around each pixel to be averaged, and compares it to the surrounding neighborhoods. It then performs a weighted average of the pixel neighborhoods, with higher weights expressing a higher degree of similarity. This principle allows effective image denoising, preserving sharp edges and avoiding excessive flattening with consequent loss of gradients. The NL-means method requires choosing the size of the neighborhood $N$, the search area dimension $\Omega$ (which defines the extent of the search for similar neighborhoods), and a noise parameter $h$, related to the level of noise in the signal. The displacement fields of Fig. 4(a) and (b) were initially denoised with the NL-

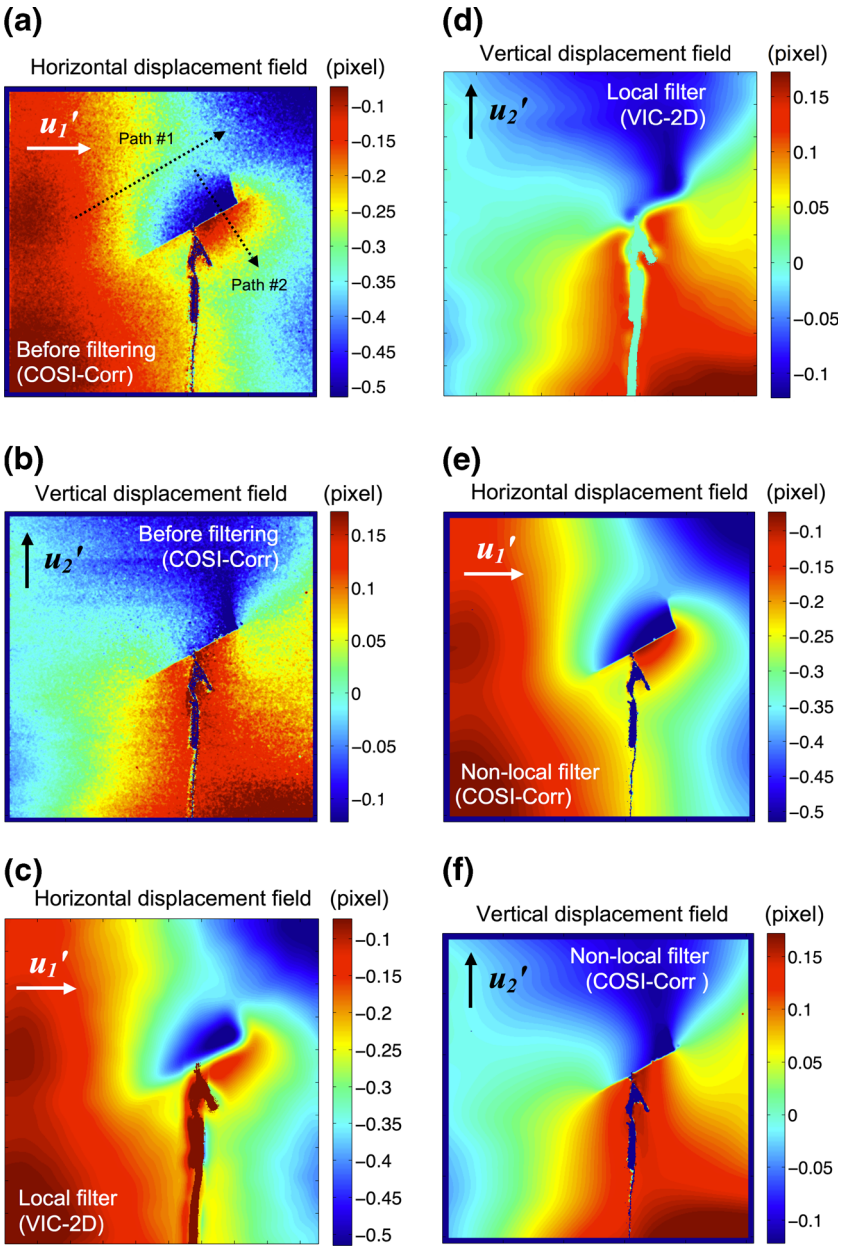


**Fig. 4** The full-field static displacement of a dynamic rupture that propagated at sub-Rayleigh speeds (applied load $P$=5 MPa): (**a**) horizontal and (**b**) vertical displacement fields. Correlation analysis is performed with COSI-Corr employing a subset size of 32 pixels and a step of 4. (c) The horizontal and (d) vertical displacement fields filtered with the Gaussian decay filter available in VIC-2D using a window of 39×39 pixels. (**e**) The horizontal and (**f**) vertical displacement fields filtered with the Non-Local Means Filter tool available in COSI-Corr. The data of (a) and (b) are filtered twice, first with parameters $N$=5×5 pixels, $\Omega$=51×51 pixels, $h$=0.08 and a second time with $h$=0.1 and all other parameters unchanged. The filtering parameters are explained in the text

means filter (as implemented in COSI-Corr; [38]) using the parameter set $N$=5×5 pixels,[1] $\Omega$=21×21 pixels, and $h$=0.08, as a starting guess [36–38]. Strain fields have been computed from such filtered displacement fields (see paragraph below). The effect of different filtering parameters, as well as filtering twice, on the strain fields has been investigated. A larger search area dimension of $\Omega$=51×51 pixels results in smoother displacement and strain fields. During the second filtering process, the same $N$ and $\Omega$ have been used, with both a larger noise parameter ($h$=0.1 pixels) and a smaller noise parameter ($h$=0.01 pixels). Higher noise parameters result in smoother displacement fields. To quantify this effect, the displacement magnitude has been tracked along pre-defined paths and compared for different noise parameters. These plots facilitate comparison between sets of filtering parameters and allow us to optimize parameter choice. The resulting displacement fields are shown in Fig. 4(e) and (f). The comparison between the filtered and unfiltered displacement signals is given in Fig. 5(a) and (b), where the horizontal displacement is tracked along the paths marked in Fig. 4(a) as Path #1 and Path #2.

Strains are computed from the displacement fields using either the central difference scheme or the multiple linear regression approach. In the central difference approximation,

[1] The pixels referred to in this section are the pixels of the displacement field images, 512 × 510 pixels, resulting from the correlation analysis, not to be confused with the pixels of the original images, 2,048 × 2,040 pixels.

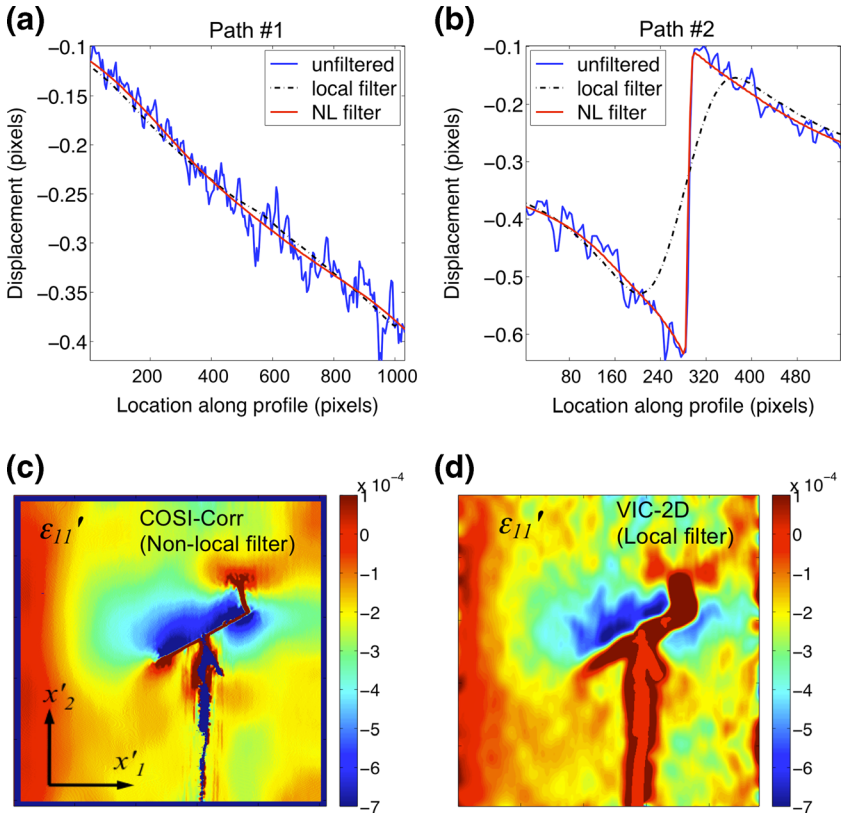


**Fig. 5** Comparison of local and non-local filtering of signals for the case of rupture that propagated at sub-Rayleigh speeds. (Top panels) The horizontal displacement value (expressed in pixel) along the paths marked in Fig. 3a: (**a**) Path # 1, (**b**) Path # 2. (Bottom panels) (**c**) The full-field map of the normal strain in the horizontal direction computed from the displacement fields obtained in COSI-Corr; the displacements are filtered with the Non-Local Means filter [24]. (**d**) The full-field map of the normal strain in the horizontal direction computed in VIC-2D; the displacements are filtered with a local filter

the normal and shear strains are expressed in the $x_1'$-$x_2'$ reference system as:

$$\varepsilon_{11}'(i,j) \cong \frac{u_1'(i,j+1) - u_1'(i,j-1)}{2\ s}$$

$$\varepsilon_{22}'(i,j) \cong -\frac{u_2'(i+1,j) - u_2'(i-1,j)}{2\ s} \quad (1)$$

$$\varepsilon_{12}'(i,j) \cong \frac{1}{2}\left\{-\frac{u_1'(i+1,j) - u_1'(i-1,j)}{2\ s} + \frac{u_2'(i,j+1) - u_2'(i,j-1)}{2\ s}\right\}$$

where $u_1'(i, j)$ and $u_2'(i, j)$ represent the generic elements of the horizontal and vertical displacement matrices, respectively, and $s$ is the step size (here $s$=4 pixels). The negative sign in the expression of the normal strain $\varepsilon_{22}'(i, j)$ and in the first term of the shear strain $\varepsilon_{12}'(i, j)$ is due to the $x_2'$axis pointing upward, and the index $i$ taking increasing values downward. In this approximation, only first-order terms are considered. Strains have been also computed including the second-order terms but no significant difference has been noticed. So all strain fields discussed henceforth neglect the second-order and higher terms. An example of the normal strain field $\varepsilon_{11}'$ is given in Fig. 5(c); the strain map is computed from the displacement field exported out of COSI-Corr, with the displacements filtered in COSI-Corr with the Non-Local-Means filter. Fig 5(d) shows that the same strain field computed by VIC-2D, with the displacements filtered in VIC-2D using a local filter, contains too much smoothing and does not capture important features close to the simulated fault. Note that the displacement fields obtained from VIC-2D can be exported out and filtered with the Non-Local-Means filter. Strain maps computed from these displacement fields are able to capture important strain features (see section "Analysis of Displacement, Strain, and Stress Fields for Sub-Rayleigh and Supershear Rupture Cases" and Fig. 10(d)). This example shows that using a non-local filter to smooth displacement fields before computing strains is a key step in obtaining meaningful strain fields, in the presence of discontinuities in the displacement field. Note that these fields are strain changes from the configuration that has already been strained by pre-loading.

Strains have also been computed by fitting the filtered displacement fields $u_1'(x_1',x_2')$ and $u_2'(x_1',x_2')$ over $m$ x $m$

pixel regions, with a multiple linear regression of the form $u_1'(x_1',x_2') \cong a+bx_1'+cx_2'$ and $u_2'(x_1',x_2') \cong \overline{a}+\overline{b}x_1'+\overline{c}x_2'$. At pixel $(i,j)$, the strains are given by: $\varepsilon_{11}'(i,j)=b$, $\varepsilon_{22}'(i,j)=-\overline{c}$ and $\varepsilon_{12}'(i,j)=\left(-c+\overline{b}\right)/2$. A larger $m \times m$ patch provides more averaging but too large a patch would lead to loss of spatial resolution. It is found that a region of 3 × 3 npixels gives the best compromise between strain resolution and displacement smoothing. The two approaches of strain calculation, central difference scheme and multiple linear regression, lead to the same results.

For the analysis in the following section, the displacement and strain fields have been rotated into the fault-related $x_1-x_2$ reference system. The stresses are obtained from the strains by employing the standard plane-stress relations with the Young's modulus $E$=3,860 MPa and Poisson's ratio $\upsilon$=0.35 [39].

## Analysis of Displacement, Strain, and Stress Fields for Sub-Rayleigh and Supershear Rupture Cases

The static field of a dynamic frictional rupture is mapped for two rupture speed regimes: sub-Rayleigh and supershear. The rupture speed regime is controlled by the interface friction, the specimen geometry (inclination angle  ), and the external applied load $P$. By employing the same specimen geometry and interface preparation as used in the present work, Gabuchian et al. [29] showed, with photoelastic and laser velocimetry techniques, that sub-Rayleigh and supershear rupture speeds are observed with external applied loads of $P$=5 MPa and $P$=15 MPa, respectively, and these load levels are applied to the test specimen in the present study.

### Static Fields of Sub-Rayleigh Rupture ($P$=5 MPa, $\alpha$ =29°)

The full-field fault-parallel and fault-normal components of the static displacement obtained by performing a correlation with COSI-Corr are shown in Fig. 6(a) and (b), respectively. The displacement fields, obtained in pixel units, are multiplied by the pixel size (i.e. 80.6 μm/pixel). In what follows, the displacement fields are expressed in μm, unless otherwise specified.

The fault-parallel component of displacement features a displacement jump (slip) across the central part of the interface up to about 47 μm (Fig. 6(c)). In contrast, there is no slip across the glued regions of the interface. When the rupture reaches the upper right edge of the frictionally held region, it forms a secondary opening crack (also called a wing crack or tailcrack) inclined at an angle of $\theta_t \approx 75°$ with respect to the fault line. The absence of a wing crack at the bottom left edge of the frictionally held region is attributed to the effect of two causes: (i) The irregular spreading of the glue on the left end of

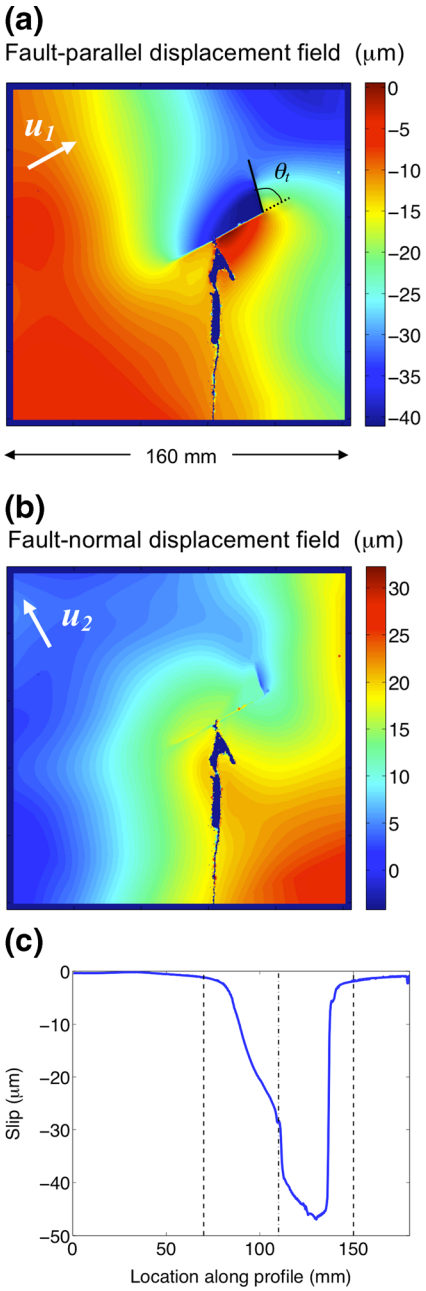


**Fig. 6** Full-field static displacement of a dynamic rupture that propagated at sub-Rayleigh speeds (applied load $P$=5 MPa). (**a**) Fault-parallel and (**b**) fault-normal displacement fields obtained by filtering and rotating the correlation results from COSI-Corr. The fault-parallel displacement field displays a maximum slip of~40 μm. The glued regions act as a barrier for rupture propagation. Note the wing crack that results from an abrupt rupture arrest. The fault-normal displacement field shows no significant discontinuity across the interface, indicating a pure mode II rupture. (**c**) The relative fault-parallel displacement (slip) along the fault. The left and right dashed lines indicate the planned ends of the frictional regions; clearly, the glue extended into the frictional region, arresting the rupture sooner. The dash-dotted line corresponds to the position of the rupture initiation; the rapid accumulation of slip in that location corresponds to a small off-fault opening crack created by the explosion

the frictionally held interface creates a more gradual transition from frictional to glued interface, since the glue is not introduced sharply through the specimen's thickness, but it is rather spread over a finite width, and (ii) the presence of a secondary crack at the hypocenter, where the rupture is nucleated by means of electrical discharge through a NiCr wire, partially relieves the high tensile strain below the left part of the interface. The fault-normal component is nearly continuous across the interface, indicating a pure mode II rupture. It is noted that most of the deformation occurs at the upper right corner of the specimen as a downward displacement, while the specimen's left edge has minimal deformation (Fig. 4). This is explained by the different boundary conditions at the two lateral edges. As mentioned in section "How to Make Earthquakes in the Laboratory", while the right edge is free, the presence of the anti-buckling bolts close to the left edge locally constrains the motion of the specimen, resulting in near-zero motion there (Figs. 4 and 6). Although the array of bolts is intended to constrain the out-of-plane motion, it is clear from our measurements that it also constrains the in-plane motion in this particular experiment. During the pre-loading stage, the vertical compression with load $P$ creates horizontal extension, due to Poisson's effect, which is non-symmetric, as the left edge does not move, and the right edge has a positive horizontal displacement. When the dynamic rupture releases some of the deformation, the right edge moves in the negative horizontal ($x_1'$) direction, while the left edge is again constrained. That is why all the horizontal displacements in Fig. 4(a) are negative, which makes the fault-parallel displacements in Fig. 6(a) negative as well. Yet, the displacement discontinuity (slip) across the rupture interface is clearly present (Fig. 6(c)). The slip profile exhibits a jump at the location of the hypocenter (dashed dotted line in Fig. 6(c)) and a further increase of slip to the right of the hypocenter. These features are caused by a combination of effects from two secondary cracks, one below the hypocenter and one at the right edge of the frictional segment, both of which serve to increase the relative interface motion to the right of the hypocenter.

The normal and shear strain fields in the $x_1$-$x_2$ reference system (Fig. 7) show two prominent near-fault regions of compressional fault-parallel strain $\varepsilon_{11}$(deep blue, Fig. 7(a)), as expected. One region of extensional fault-parallel strain, though smaller, is present on the left part of the interface, again as expected (Fig. 7(a), red). The other expected extensional region above the interface is replaced by a wing crack, with the red color at its tip signifying the tensile strain concentration there. The deviations from anti-symmetry are attributed to the lack of symmetry in the pre-stress field, boundary conditions, and glued interface (the glue forming an irregular boundary on the interface, as shown in Fig. 2(b)), and the formation of two off-interface cracks, one wing crack and the other crack in the wire channel area. The non-symmetric glued

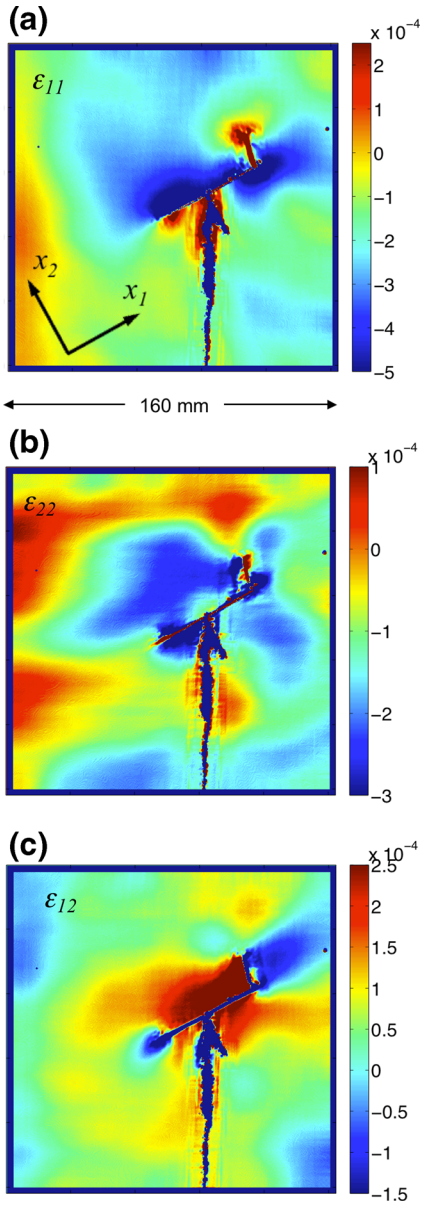


**Fig. 7** Full-field static strain maps of a dynamic rupture that propagated at sub-Rayleigh speeds (applied load $P$=5 MPa): (**a**) fault-parallel, (**b**) fault-normal, and (**c**) shear strain field. The strain in the fault-parallel direction displays a compressive pattern anti-symmetrically with respect to the interface. The anti-symmetric extensional pattern is less pronounced due to the stress release at the wing crack (above the interface) and to the presence of the alligator clips (below the interface)

interface is also responsible for the formation of one wing crack (instead of two). A closer inspection of the glued interface reveals that the glue on the higher end of the interface forms a sharper edge so the rupture arrest is abrupt and a wing crack forms on the extensional side of the rupture. In contrast, the lower end of the glued interface is less sharp and provides a more gradual rupture arrest zone, preventing the wing crack there. The formation of a wing crack has the effect of releasing locally tensile strains. So the extensional lobe expected to the upper right of the

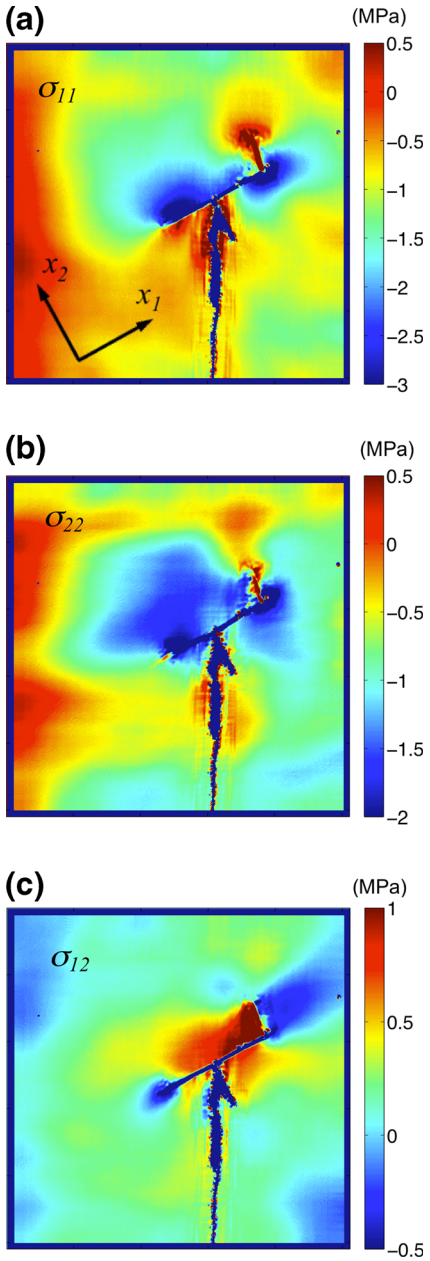


**Fig. 8** Full-field static stress maps of a dynamic rupture that propagated at sub-Rayleigh speeds (applied load $P$=5 MPa): (**a**) fault-parallel, (**b**) fault-normal directions, and (**c**) shear stress field

interface is not present. Tensile strains, however, are concentrated at the tip of the secondary crack. Similarly, the crack at the hypocenter partially relieves the tensile strains below the left part of the interface, decreasing the expected tensile strains there and increasing the compressive lobe to the right.

Normal strains in the fault-normal direction $\varepsilon_{22}$ (Fig. 7(b)) would tend to be tensile in the regions that experience compressional strains in the fault-parallel $x_1$ direction, due to Poisson's effect. However, the confinement of the neighboring material induces a state of compression instead. A positive shear strain $\varepsilon_{12}$ (Fig. 7(c)), consistent with the counter-clockwise shearing deformation of the specimen, is seen in a broad region around the interface. The negative shear strains around the rupture tips are due to the constraints imposed by the neighboring material arresting the rupture.

Normal and shear stress fields, plotted in the $x_1$-$x_2$ reference frame, are shown in Fig. 8. The normal stress maps are similar to the normal strain maps since the dominant component in $\sigma_{11}$ and $\sigma_{22}$ are $\varepsilon_{11}$ and $\varepsilon_{22}$, respectively. Likewise, the shear stress field is consistent with the shearing of the material around the interface and displays stress concentrations at the crack tips. The shear stress field change around the interface is of the order of 1 MPa. This quantity, called "stress drop", is important in seismology. This value is consistent with the prediction of an analytical formula for a 2D crack embedded in a plane-stress medium:

$$\Delta\tau = C\mu\frac{\overline{\delta}}{2a}, \tag{2}$$

where $C$ is a coefficient of order 1, $\overline{\delta}$ is the magnitude of average slip and $2a$ is the crack length. Using the left side of the frictional interface, which is not affected by a wing crack, one estimates $\overline{\delta} = 15$ μm, $a$=20 mm, and hence $\Delta\tau \cong$ 0.55 MPa.

Static Fields of Supershear Rupture ($P$=15 MPa, $\alpha$ =29°)

The unfiltered fault-parallel and fault-normal components of displacement obtained with COSI-Corr are shown in Fig. 9(a) and (b) respectively. The central region of the upper plate exhibits a negative (downward) fault-parallel displacement in excess of 200 μm, while the central region of the lower plate has a positive (upward) displacement of about 400 μm. Since this rupture propagates under higher loading and with higher stress changes, the motion involved is much stronger and the effect of the bolts on constraining the lateral displacement of the left edge is significantly reduced. The fact that the rupture transitions to supershear speeds further intensifies the motion. The fault-normal displacement field shows no significant discontinuities across the interface, indicating a pure mode II crack. Two wing cracks extend from where the rupture fronts hit the glued boundaries. The wing cracks form two kink angles with respect to the interface of $\theta_t^{(u)} \approx 70°$ (upper wink crack) and $\theta_t^{(l)} \approx 75°$ (lower wink crack). It is noted that the wing crack path is curved. As expected, the wing crack propagation stops once the crack path is aligned with the direction of compression.

The inferred full-field strain maps are shown in Fig. 10. Prior to computing the strains, the displacement fields are filtered according to the procedure described in section "Data Post-Processing: Displacement Filtering, Strain and Stress Calculation". When the rupture reaches the glued boundaries,

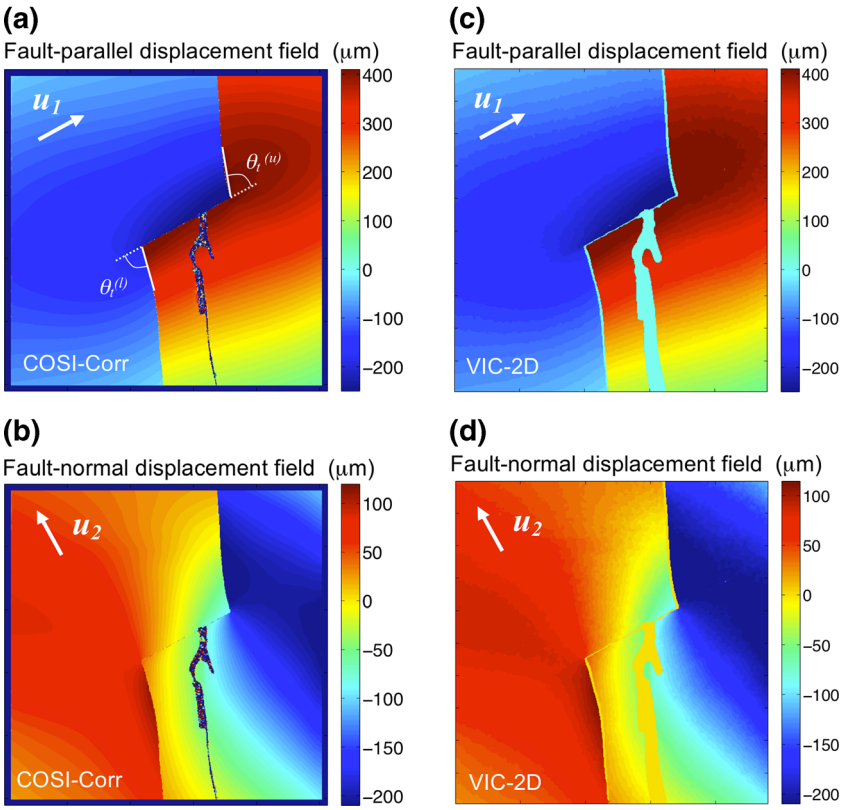


**Fig. 9** Full-field static displacement of a dynamic rupture that propagated at supershear speeds (applied load $P$=15 MPa). (**a**) Fault-parallel and (**b**) fault-normal displacement fields obtained by rotating the correlation results from COSI-Corr; (**c**) fault-parallel and (**d**) fault-normal displacement fields obtained by rotating the correlation results from VIC-2D. The fault-parallel displacement field displays a maximum slip in excess of ~600 μm. The glued regions arrest the rupture on both the upper and lower end. Note the wing cracks forming on the extensional sides of the rupture as a result of the abrupt rupture arrest. The fault-normal displacement field shows no significant discontinuity across the interface, indicating a pure mode II rupture

it forms wing cracks on the extensional sides. Two wing cracks are formed this time, as both glued edges are sharp and stress changes involved are higher due to higher loading. The strain fields are complex, reflecting both the interface rupture and dominating effects of two curved wing cracks which are larger than the initial interface rupture. Shear strain,

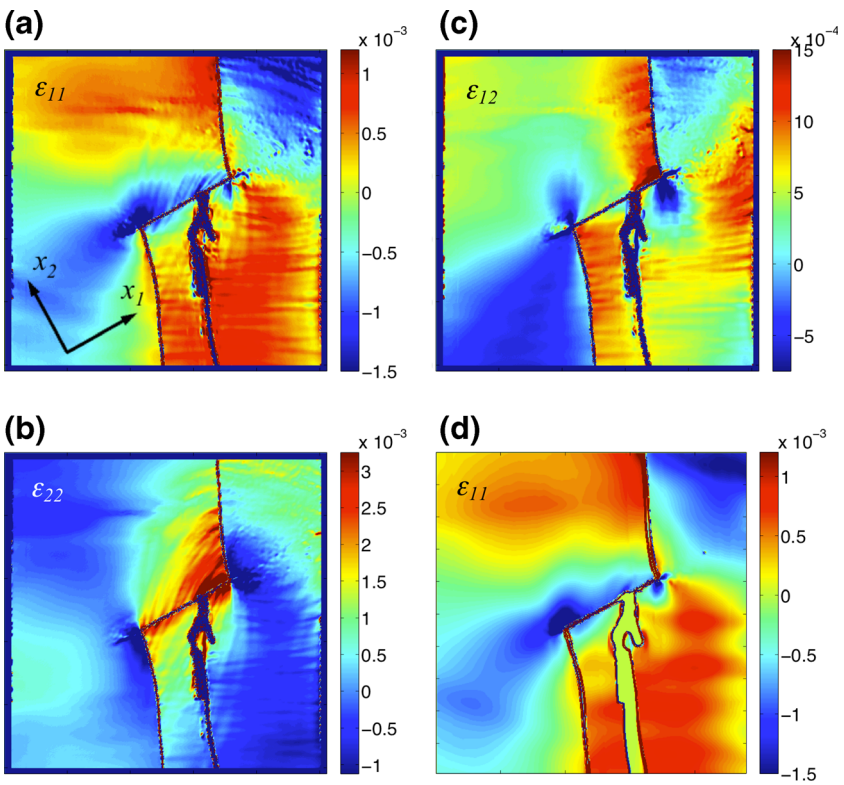


**Fig. 10** Full-field static strain maps of a dynamic crack that propagated at supershear speeds (applied load $P$=15 MPa): (**a**), (**d**) fault-parallel, (**b**) fault-normal, and (**c**) shear strain field. The strains in (a-c) are computed from the displacement fields obtained using COSI-Corr, and the strain in (d) is computed from the displacement fields obtained using VIC-2D. Unlike for Fig. 5(d), the displacements used for panel (d) are filtered with the NL-means filter, as done in COSI-Corr. As the strain is released with the formation of secondary cracks, the extensional sides become less pronounced in the plot. The full-field strain maps are able to capture singularities at the crack tips

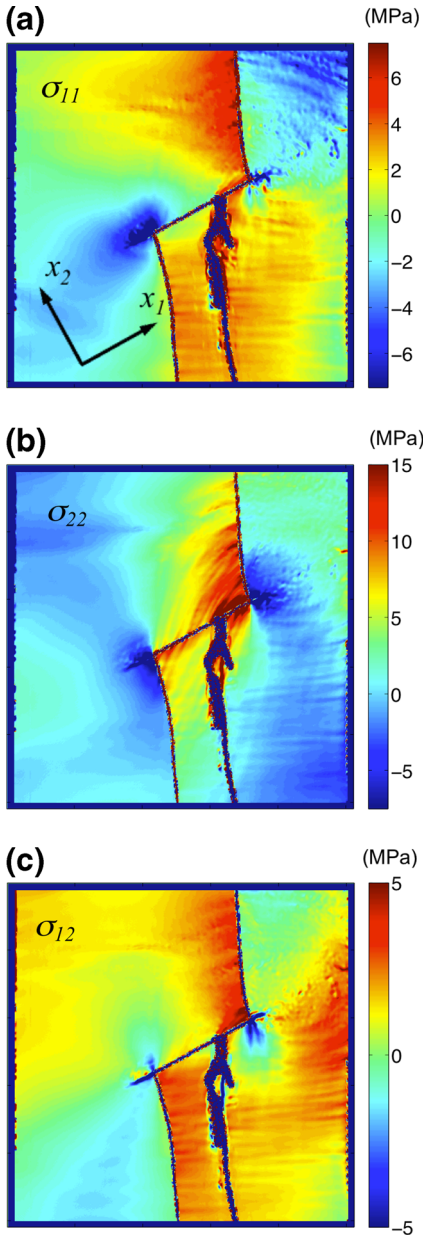


**Fig. 11** Full-field static stress maps of a dynamic crack that propagated at supershear speeds (applied load $P$=15 MPa): (**a**) fault-parallel, (**b**) fault-normal, and (**c**) shear stress field. Note that the two wing cracks, as expected, form on the extensional sides of the rupture. Despite the stress release during the wing cracks propagation, tensile stresses are still visible on the upper and (less pronounced) lower wing crack

shown in Fig. 10(c), is approximately anti-symmetric. The positive regions reflect the plate shearing while the negative regions correspond to the rupture arrest. Strain concentrations at the tips of the rupture are clearly visible. Full-field stress plots are reported in Fig. 11. Normal stress $\sigma_{11}$ reveals the compressional quadrant at the lower end of the interface, while the compressional quadrant at the upper end is masked by higher tensile stresses in the lower plate. The extensional quadrants create the wing cracks and, as the cracks propagate, the stress is released. Note that our interest is in studying the main (interface) crack and our future experimental design will include gradual transition from the frictional to glued interface, to prevent wing crack from forming.

Secondary (or wing) crack growth in brittle materials under compression has been observed by several authors (e.g. [40–42]) and it has been shown that secondary cracks grow along a curved path, which becomes parallel with the direction of compression. The curved crack path is due to the crack growing in a non-uniform stress-field. Brace and Bombolakis [40] report some early observations on crack growth in photoelastic materials used to investigate brittle fracture of rocks. Analytical models of wing crack mechanics have been subsequently developed [41–47]. For example, Willemse and Pollard [47] present analytical solutions for the kink angle based on linear fracture mechanics (LEFM) and cohesive end zone (CEZ) flaw models. They show that LEFM predicts tensile cracks extensions at an angle close to 70° from the direction of the parent crack, with overall compressive stress conditions (i.e. no opening mode singularity), while CEZ predict significantly lower angles. The authors argue that the most appropriate description (LEFM or CEZ) depend on the boundary conditions that accompany sliding. We found kink angles close to $\theta_t \approx 70°$, consistently with the LEFM analytical predictions. Angles higher than 70° may be due to non-uniform boundary of glue across the plate thickness (also leading to a through thickness crack twist) and, in the case of the lower angle in Fig. 9, may be due to the effect of the bolts in proximity of the specimen's left edge, which partly constrain the in-plane motion at the left edge (Fig. 2(b)).

## Comparison between COSI-Corr and VIC-2D

A comparison of the digital image correlation analysis obtained with VIC-2D and COSI-Corr is given in Fig. 9. Despite some minor differences, the displacement fields obtained with the two software packages are in good agreement overall. A slightly more elaborate procedure is necessary to produce VIC-2D results. VIC-2D requires the user to specify a starting point for the correlation procedure. In some cases, such as the example discussed in this section, the analysis outcome is dependent on where the initial point is selected, while COSI-Corr has no such requirement. In this example, the starting point is selected to be on the bottom plate, between the wire and opening crack. With this selection, the program automatically excludes from the correlation a small region around the wire, which cannot be correlated between the images, as the wire is absent in the image after deformation (Fig. 3). If a different choice is made, however, the correlation would only converge on a portion of the specimen.

The importance of filtering displacement fields prior to computing strains with a non-local filter is emphasized in section "Data Post-Processing: Displacement Filtering, Strain and Stress Calculation" (Fig. 5). COSI-Corr, which was

developed to deal with displacement offsets occurring in earthquake problems, implements the Non-Local Means filter of Buades et al. [36] in order to preserve discontinuity features while smoothing the displacement fields. The strains computed from the displacement fields of COSI-Corr filtered with the Non-Local means filter capture important features even in the presence of displacement discontinuities (section "Data Post-Processing: Displacement Filtering, Strain and Stress Calculation"; Fig. 5(c), 7, and 10). In contrast, VIC-2D implements local filters, so the discontinuities are not clearly preserved when smoothing the displacement fields (Fig. 5(b)), and the strains computed from such displacements do not capture accurately the displacement gradients (Fig. 5(d)).

The displacement fields obtained from VIC-2D can alternatively be exported and filtered with the NL-means filter (implemented outside of the COSI-Corr framework), using the same procedure employed with COSI-Corr. An example of the normal strain in the fault-parallel direction computed following this approach is shown in Fig. 10(d), using the same source images as for Fig. 10(a)-(c) (supershear case). While the main strain pattern is captured, some small-scale features present in Fig. 10(a) are not present in Fig. 10(d). Note that approximately the same subset size is used to run the correlation analysis in VIC-2D (31 × 31 pixels; VIC-2D requires the subset size to be an odd number) as in COSI-Corr (32 × 32 pixels; COSI-Corr requires the subset size to be a power of two), and the same filtering parameters are used to filter the displacement fields. However, the NL-means filter implemented outside of the COSI-Corr framework has an effective noise parameter $h$ larger than the equivalent parameter in the COSI-Corr implementation. As a result, the strain field computed from VIC-2D data (Fig. 10(d)) is smoother than that obtained from COSI-Corr (Fig. 10(a)).

## Accuracy of the DIC Measurements for Laboratory Earthquakes

The accuracy of the method is affected by a number of factors: the interpolation method, the shape function order, the intensity of the pattern noise, and the subset size. (e.g. [48–52]). One way to assess the accuracy of the DIC method is by translating the target images by a known amount and comparing the input displacement to the measured displacement. The target images can either be shifted numerically (by using the Fourier's shift theorem) or by translating the specimen

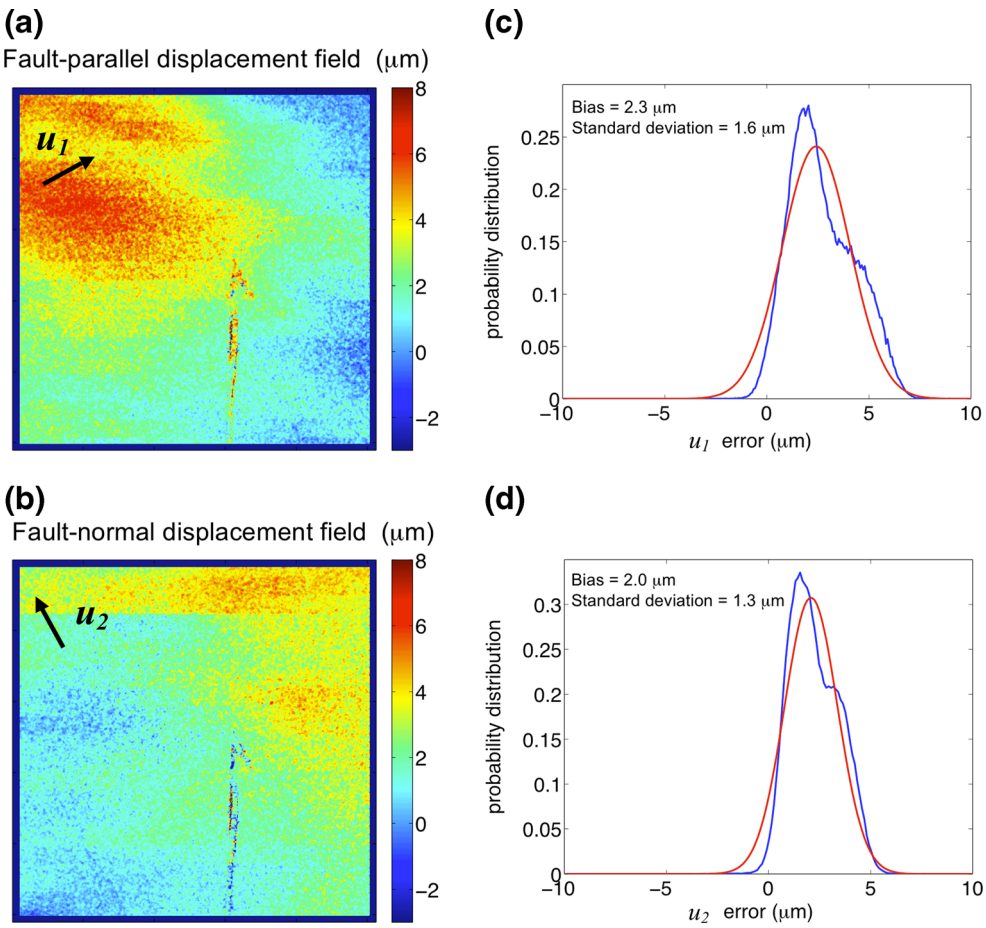


**Fig. 12** (**a**) Fault-parallel and (**b**) fault-normal displacement fields obtained by correlating two nominally identical images with COSI-Corr. Correlating two nominally identical images gives a scale for the measurements error. The correlation analysis is performed with the same parameters as those used for the above analysis. Subset size: 32, Step: 4. Probability distribution function of the (**c**) fault-parallel and (**d**) fault-normal maps (*blue curves*). A gaussian fit (*red curve*) is added to infer bias and standard deviation

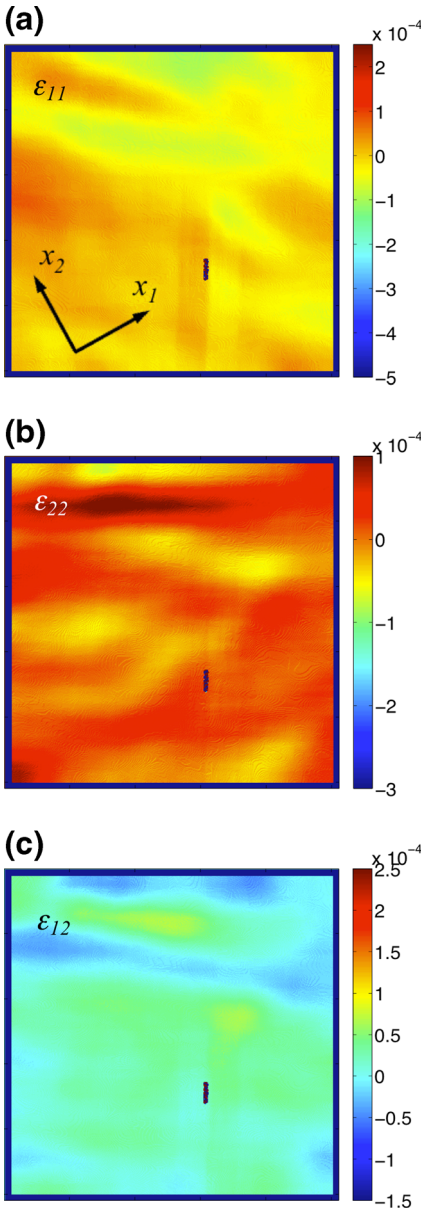


**Fig. 13** (**a**) Fault-parallel, (**b**) fault-normal and (**c**) shear strain fields obtained by filtering and differentiating the displacement fields of Fig. 12. The strain level due to noise is significantly lower than strain measured during the experiments presented here

with a calibrated stage. The errors measured by shifting the images numerically quantify the errors due to interpolation at sub-pixel locations. This procedure does not account for other sources of error such as camera noise and intensity of the pattern noise. On the other hand, translating the specimen on a stage has the shortcoming of the input displacement uncertainty. While interpolation errors can be significantly reduced by using appropriate interpolation functions (e.g. [14, 48]), we would like to quantify the errors due to the camera noise, intensity of the pattern noise, and micro vibrations of the measuring system, as they likely give the largest contribution to the measurement error in this setup.

Two independent images of the specimen with no load applied are taken. The displacement and strain fields associated with the correlation of the two nominally identical images are then computed. The discrepancies of the displacement and strain fields from zero provide a measure of the error. The displacement fields obtained by correlating two nominally identical images with COSI-Corr are shown in Fig. 12(a) and (b), in the fault-parallel and fault-normal directions, respectively. The subset size and step size are 32×32 and 4 pixels, respectively (the same as those employed in "Analysis of Displacement, Strain, and Stress Fields for Sub-Rayleigh and Supershear Rupture Cases"). The probability distribution functions (*blue curves*) are shown in Fig. 12(c) and (d); Gaussian fits (*red curves*) to the probability distributions are also displayed in the same plots. The bias and standard deviation associated with the normal distributions give a scale of the systematic and random errors of the measurements. The fault-parallel component has the largest values: the bias is 2.4 μm and the standard deviation is 1.7 μm (which correspond to approximately 3/100 and 2/100 of a pixel). The analysis of the same images with VIC-2D gives very similar error results.

A comparison of these values with the measured displacement of Fig. 6 (the example with the smaller maximum displacements) shows that meaningful displacement measurements are possible in this setup, since displacements are in the tens of microns while the displacement accuracy is of about a few microns. Likewise, the strain errors (Fig. 13), computed by filtering and differentiating the displacement errors (Fig. 12(a) and (b)), are significantly smaller than the smallest strains measured in this study (Fig. 7), indicating that meaningful strain measurements are indeed possible.

The error measurement procedure has also been used to determine the optimum subset and step sizes. Correlations performed with a smaller subset size lead to a loss of accuracy while increasing the subset size causes a loss of resolution. So the optimum subset size is determined to be 32 × 32pixels. Correlations performed with a step size larger than 4 pixels would display a decreased data density, while decreasing the step size to less than 4 would significantly increase computation times.

Different speckle patterns containing features of different size and density have been analyzed to determine the optimum pattern for this study. The pattern of Fig. 3 is found to minimize the displacement and strain errors. This is attributed to the fact that patterns with sparser features would lead to large regions without a gray level variation, while too dense patterns would result in black-saturated patches. Producing the speckle pattern by spraying the specimen surface does not allow for a fine control of the feature size but it allows us to produce gray level variations which are suitable to be analyzed with the DIC method and produce reasonably accurate results.

To study the effect of filtering on the error, the displacement fields of Fig. 12 are filtered, following the same

procedure outlined for the displacement fields of the above examples. Similar plots to those of Fig. 12(c) and (d) are produced for the filtered signals (not shown here). It is noted that the standard deviation is reduced, while the bias is unvaried, as expected. The filtered displacement fields are used to compute the strain fields (Fig. 13). Since the strain errors are significantly smaller than the strains measured in either of the two tests presented here, it is concluded that accurate strain measurement is possible in this setup.

## Concluding Remarks and Discussion

The full-field static displacement of a laboratory earthquake rupture has been successfully characterized with two DIC software packages: VIC-2D and COSI-Corr. Two rupture speed regimes have been investigated: sub-Rayleigh and supershear. The correlation analysis performed with either software clearly shows (i) the relative displacement (slip) along the frictional interface, (ii) the rupture arrest on the glued boundaries, and (iii) the presence of wing cracks. Displacements are processed using de-noising techniques and strains are subsequently computed using two alternative approximations: central-difference scheme and multiple linear regression. The full-field strain maps computed with either approach, together with the stress maps, reveal the extensional and compressional state along the ruptured interface. The displacement fields contain enough resolution to capture strain and stress concentration at the rupture tip. Slip along the interface as well as the shear stress drop can be inferred from the obtained results.

A key step in obtaining meaningful strain and stress fields is appropriately filtering the displacement fields. COSI-Corr implements an effective non-local filter which allows to smooth displacement fields while preserving discontinuities in the data. The strain maps computed from the displacement maps filtered by the non-local filter capture important features of the deformation field. In contrast, the local filters available in VIC-2D are not suitable for cases with displacement discontinuities as they average displacement values across the discontinuity and prevent accurate computation of displacement gradients in the proximity of such boundaries. However, the displacement data computed by VIC-2D can be exported and post-processed outside the VIC-2D software with a non-local filter, to produce similar results to those obtained with COSI-Corr.

The adopted technique to glue a portion of the interface can be used in a systematic study of crack arrest, as one possible technique to arrest ruptures. Another technique would comprise a transition zone from glued to purely frictional interface in order to have a gradual arrest of the rupture. This could be achieved by gauging the amount of glue from a sparser to a denser pattern of glue spots. On the other hand, an abrupt rupture arrest, producing secondary cracks, such as the one featured in this study, is not unrealistic. Indeed, secondary cracks have been observed forming on opposite tips of a fault, as a consequence of the faulting process [46, 53–58]. Kinked crack extension under overall far-field compression has explained a number of geological phenomena, such as splitting, exfoliation and rockburst [42]. Secondary crack extension has not only been observed in geological phenomena but also in planetary science. For example, wing cracks at the tips of strike-slip faults have been observed on the ice shell of Jupiter's moon, Europa [59].

The method accuracy has been studied by correlating two nominally identical images. The statistical properties of the measured signal are used to quantify the error associated with the measurements. The bias is of the order of 2.4 μm and the random error is of the order of 1.7 μm, when the correlation is performed with COSI-Corr. Similar values are obtained with VIC-2D. Overall, the error analysis reveals that the digital image correlation technique as implemented in the laboratory earthquake setup discussed here is capable of capturing displacements of the order of (or larger than) 10 μm, while errors in the order of up to few microns are expected. Smaller displacements can be captured with a higher magnification factor, at the cost of a smaller field of view for a given camera resolution.

Existing remote sensing techniques allow to measure the co-seismic deformation, with pre- and post-earthquake images offering an invaluable tool to understand the earth deformation. However, they lack the capability of capturing highly transient phenomena. The "space optical seismometer" is a new concept that would allow capturing full-field optical satellite images during a seismic event over a wide area, providing a unique opportunity to monitor the evolution of the Earth's surface [28]. The concept is based on a geostationary satellite optical telescope with a high-density spatio-temporal sampling. While theoretical and numerical simulations indicate that the concept of space optical seismometer should be possible [28], it is important to demonstrate the feasibility of the concept with experiments. We plan to couple the DIC technique with high-speed photography in order to obtain the temporal evolution of the full-field displacement and strain during the rupture process. The error analysis of our preliminary static measurements suggests that useful dynamic measurements should be feasible with the present instrumentation, in an area of about 2 by 2 cm. This would be sufficient for characterizing the evolution of slip and slip rate in areas of interest, such as interaction of rupture with a heterogeneous patch or a branch.

**Acknowledgement** We gratefully acknowledge the support for this study from the National Science Foundation (grant EAR 1142183 and 1321655), the Gordon and Betty Moore Foundation (through Tectonic Observatory at Caltech and grant GBM 2808), the Southern California Earthquake Center (SCEC), and the Keck Institute for Space Studies. This is Tectonics Observatory contribution #250 and SCEC contribution #1810.

## References


1. Leprince S, Barbot S, Ayoub F, Avouac J-P (2007) Automatic, precise, ortho-rectification and co-registration for satellite image correlation, application to seismotectonics. IEEE Trans Geosci Remote Sens 45(6):1529–1558
2. Leprince S, Ayoub F, Klinger Y, Avouac J-P (2007) Co-Registration of Optically Sensed Images and Correlation (COSI-Corr): an Operational Methodology for Ground Deformation Measurements. IEEE International Geoscience and Remote Sensing Symposium (IGARSS 2007), Barcelona July 2007
3. Rosakis, AJ, Xia KW, Lykotrafitis G, Kanamori H (2007) Dynamic shear rupture in frictional interfaces: speeds, directionality and modes, Treatise in Geophysics, edited by H. Kanamori, vol. 4, 153–192
4. Okada Y, Kashara K, Hori S, Obara K, Sekiguchi S, Fujiwara H, Yamamoto A (2004) Recent progress of seismic observation networks in Japan—Hi-net, F-net, K-NET and KiK-net. Earth Planet Space 56:15–28
5. Massonnet D, Feigl KL (1998) Radar interferometry and its application to changes in the earth's surface. Rev Geophys 36(4):441–500
6. Van Puymbroeck N, Michel R, Binet R, Avouac JP, Taboury J (2000) Measuring earthquakes from optical satellite images. Appl Opt 39: 3486–3494
7. Kaab A (2002) Monitoring high-mountain terrain deformation from repeated air—and spaceborne optical data: examples using digital aerial imagery and ASTER data. ISPRS J Photogramm 57(1–2):39–52
8. Rosakis AJ, Samudrala O, Coker D (1999) Cracks faster than the shear wave speed. Science 284:1337–1340
9. Rosakis AJ (2002) Intersonic shear cracks and faults rupture, adv. Phys 51(4):1189–1257
10. Xia K, Rosakis AJ, Kanamori H (2004) Laboratory earthquakes: the sub-Rayleigh-to-supershear rupture transition. Science 303:1859–1861
11. Xia K, Rosakis AJ, Kanamori H, Rice J (2005) Laboratory earthquakes along inhomogeneous faults: directionality and supershear. Science 308:681–684
12. Lu X, Lapusta N, Rosakis AJ (2007) Pulse-like and crack-like ruptures in experiments mimicking crustal earthquakes. Proc Natl Acad Sci U S A 104:18931–18936
13. Lu X, Lapusta N, Rosakis AJ (2009) Analysis of supershear transition regimes in rupture experiments: the effect of nucleation conditions and friction parameters. Geophys J Int 177: 717–732
14. Sutton MA, Orteu J-J, Schreier HW (2009) Image correlation for shape, motion, and deformation measurements. Springer
15. Peters WH, Ranson WF (1982) Digital image technique in experimental stress analysis. Opt Eng 21:427–431
16. Sutton MA, Wolters WJ, Peters WH, Ranson WF, McNeill SR (1983) Determination of displacements using an improved digital correlation method. Image Vis Comput 1(3):133–139
17. Chu TC, Ranson WF, Sutton MA, Peters WH (1985) Application of digital-image correlation techniques to experimental mechanics. Exp Mech 25:232–244
18. Sutton MA, Turner JL, Chao YJ, Bruck HA, Chae TA (1991) Experimental investigations of three-dimensional effects near a crack tip using computer vision. Int J Fract 53(3):201–228
19. Abanto-Bueno J, Lambros J (2002) Investigation of crack growth in functionally graded materials using digital image correlation. Eng Fract Mech 69(14–16):1695–1711
20. Jin H, Bruck HA (2005) Theoretical development for pointwise digital image correlation. Opt Eng 44(6). doi:10.1117/1.1928908
21. Kirugulige MS, Tippur HV, Denney TS (2007) Measurement of transient deformations using digital image correlation method and high-speed photography: application to dynamic fracture. Appl Opt 46(22):5083–5096
22. Réthoré J, Roux S, Hild F (2008) Extended digital image correlation with crack shape optimization. Int J Numer Meth Eng 73(2):248–272
23. Kirugulige MS, Tippur HV (2009) Me3asurement of fracture parameters for a Mixed-mode crack driven by stress waves using image correlation technique and High-speed digital photography. Strain 45(2):108–122
24. Jajam KC, Tippur HV (2011) An experimental investigation of dynamic crack growth past a stiff inclusion. Eng Fract Mech 78(6): 1289–1305
25. Sutton MA, Cheng M, Peters WH, Chao YJ, McNeill SR (1986) Application of an optimized digital correlation method to planar deformation analysis. Image Vis Comput 4(3):143–150
26. Bruck HA, McNeill SR, Sutton MA, Peters WH (1989) Digital image correlation using Newton–Raphson method of partial differential correction. Exp Mech 29(3):261–267
27. Mello M, Bhat HS, Rosakis AJ, Kanamori H (2010) Identifying the unique ground motion signatures of supershear earthquakes: theory and experiments. Tectonophysics 493:297–326
28. Michel R, Ampuero J-P, Avouac J-P, Lapusta N, Leprince S, Redding DC, Somala S (2013) A geostationary optical seismometer, proof of concept. IEEE Transactions on Geoscience and Remote Sensing, in press
29. Gabuchian V, Rosakis AJ, Lapusta N, Oglesby D (2014) Experimental investigation of strong ground motion due to thrust fault earthquakes. J Geophys Res Solid Earth 119:1316–1336
30. Lykotrafitis G, Rosakis AJ (2006) Dynamic sliding of frictionally held bimaterial interfaces subjected to impact shear loading. Proc R Soc Math Phys Eng Sci 462:2997–3026
31. Lykotrafitis G, Rosakis A, Ravichandran G (2006) Self-healing pulse-like shear ruptures in the laboratory. Science 313(5794):1765–1768
32. Sutton MA, Turner JL, Bruck HA, Chae TA (1991) Full-field representation of discretely sampled surface deformation for displacement and strain analysis. Exp Mech 31(2):168–177
33. Sutton MA, McNeil SR, Helm JD, Chao YJ (2000) Advances in two-dimensional and three-dimensional computer vision. In: Rastogi PK (ed) Photomechnics, topics in applied physics. Springer, Berlin, pp 323–372
34. Avril S, Feissel P, Pierron F, Villon P (2010) Comparison of two approaches for differentiating full-field data in solid mechanics. Meas Sci Technol. doi:10.1088/0957-0233/21/1/015703
35. Buades A, Coll B, Morel JM (2006) The staircasing effect in neighborhood filters and its solution. IEEE Trans Image Process 15:1499–1505
36. Buades A, Coll B, Morel JM (2008) Nonlocal image and movie denoising. Int J Comput Vis 76:123–139
37. Goossens B, Luong H, Pizurica A, Philips W (2008) An improved non-local denoising algorithm. Proceedings of the 2008 international workshop on local and Non-local approximation in image processing. Lausanne, Switzerland
38. Ayoub F, Leprince S, Keene L (2009) User's guide to COSI-CORR CO-registered of optically sensed images and correlation. California Institute of Technology, Pasadena
39. Dally J, Riley W (2005) Experimental stress analysis, 4th edn. College House Enterprises, LLC
40. Brace WF, Bombolakis EG (1963) A note on brittle crack growth in compression. J Geophys Res 68:3709–3713
41. Erdogan F, Sih GH (1963) On the crack extension in plates under plane loading and transverse shear. J Basic Eng-T ASME 85:519–527
42. Nemat-Nasser S, Horii H (1982) Compression-induced nonplanar crack extension with application to splitting, exfoliation and rockburst. J Geophys Res 87:6805–6821
43. Hussain MA, Pu SL, Underwood JH (1974) Strain energy release rate for a crack under combined mode I and mode II. In: fracture Analysis. Proceedings of the 1973 National Symposium on Fracture Mechanics II. Am Soc Test Mate Spec Tech Publ 560:2–28

44. Cotterell B, Rice JR (1980) Slightly curved or kinked cracks. Int J Fract 16:155–169
45. Pollard DD, Segall P (1987) Theoretical displacements and stresses near fractures in rock: with applications to faults, joints, veins, dikes, and solution surfaces. In: Atkinson BK (ed) Fracture mechanics of rock. Academic, London, pp 277–349
46. Cruikshank KM, Zhao G, Johnson AM (1991) Analysis of minor fractures associated with joints and faulted joints. J Struct Geol 13: 865–886
47. Willemse EJM, Pollard DD (1998) On the orientation and patterns of wing cracks and solution surfaces at the tips of a sliding flaw or fault. J Geophys Res 103:2427–2438
48. Schreier HW, Braasch JR, Sutton MA (2000) Systematic errors in digital image correlation caused by intensity interpolation. Opt Eng 39(11):2915–2921
49. Schreier HW, Sutton MA (2002) Systematic errors in digital image correlation due to undermatched subset shape functions. Exp Mech 42(3):303–310
50. Lecompte D, Bossuyt S, Cooreman S, Sol H, Vantomme J (2007) Study and generation of optimal speckle patterns for DIC. 2007 SEM Proceedings
51. Wang ZY, Li HQ, Tong JW, Ruan JT (2007) Statistical analysis of the effect of intensity pattern noise on the displacement measurement precision of digital image correlation using self-correlated images. Exp Mech 47:700–707
52. Wang YQ, Sutton MA, Bruck HA, Schreier HW (2009) Quantitative error assessment in patter matching: effects of intensity pattern noise, interpolation, strain and image contrast on motion measurements. Strain 45:160–178
53. Rispoli R (1981) Stress fields about strike-slip faults inferred from stylolites and tension gashes. Tectonophysics 75:T29–T36
54. Willemse EJM, Peacock DCP, Aydin A (1997) Nucleation and growth of strike-slip faults in limestones from Somerset, U.K. J Struct Geol 19:1461–1477
55. Martel SJ, Boger WA (1998) Geometry and mechanics of secondary fracturing around small three-dimensional faults in granitic rock. J Geophys Res 103(B9):21,299–21,314
56. Younes A, Engelder T (1999) Fringe cracks: key structures for the interpretation of progressive Alleghanian deformation of the appalachian plateau. GSA Bull 111:219–239
57. Cooke M, Mollema P, Pollard DD, Aydin A (2000) Interlayer slip and fracture clusters within East Kaibab monocline: numerical analysis and field investigations. In: Cosgrove J, Ameen M (eds) Drape folds and associated fractures. Geological Society of London Special Publication, London, pp 23–49
58. Kattenhorn SA, Aydin A, Pollard DD (2000) Joints at high angles to normal fault strike: an exploration using 3-D numerical models of fault-perturbed stress fields. J Struct Geol 22:1–23
59. Kattenhorn SA, Marshall ST (2006) Fault-induced perturbed stress fields and associated tensile and compressive deformation at fault tips in the ice shell of Europa: implications for fault mechanics. J Struct Geol 28:2204–2221